CrystEngComm

RSC Publishing

PAPER

View Article Online
View Journal | View Issue

Effects of surface modification and SiO_2 thickness on the optical and superparamagnetic properties of the water-soluble ZnS:Mn^{2+} nanowires/Fe_3O_4 quantum dots/SiO_2 heterostructures

Cite this: *CrystEngComm*, 2013, **15**, 6971

Jian Cao,*[ab] Bingji Wang,[ab] Donglai Han,[cd] Shuo Yang,[cd] Jinghai Yang,*[ab] Maobin Wei,[ab] Lin Fan,[ab] Qianyu Liu[ab] and Tingting Wang[ab]

Received 28th May 2013,
Accepted 3rd July 2013

DOI: 10.1039/c3ce40939b

www.rsc.org/crystengcomm

In this paper, one-dimensional ZnS:Mn^{2+} nanowires (NWs)/Fe_3O_4 quantum dots (QDs)/SiO_2 heterostructures were successfully synthesized by the Stöber method to form the water-soluble fluorescent/superparamagnetic nanocomposites. The average diameter of the ZnS:Mn^{2+} NWs, Fe_3O_4 QDs and ZnS:Mn^{2+} NWs/Fe_3O_4 QDs/SiO_2 heterostructures was about 6–8 nm, 4–5 nm and 18 nm, respectively. The Fe_3O_4 QDs were covalently linked to the ZnS:Mn^{2+} NWs by the conjugation of the hydroxyl groups on the surface of the QDs and the carboxyl groups modified on the surface of the NWs. It was found that the covalent bonds between the NWs and QDs could effectively suppress the energy transfer from the ZnS:Mn^{2+} NWs to the Fe_3O_4 QDs. As the SiO_2 shell thickness increased, the fluorescence intensity reached the highest value when the hydrolysis time of tetraethyl orthosilicate was 5 hours, which was comparable to that of the ZnS:Mn^{2+} NWs. The superparamagnetic properties of the heterostructures were observed at room temperature, which decreased as the SiO_2 thickness increased.

Introduction

Next generation molecular probes combining magnetic and fluorescent properties in one entity open up broader avenues for their applications as dual-modality imaging probes in the fields of biological imaging, cell tracing, magnetic bioseparation, targeted drug delivery, *etc.*[1–5] Among the widely studied fluorescent labeling nanomaterials, ZnS has great advantages as follows: (1) low toxicity, (2) high photostability, (3) relative lower price, (4) simple synthesis procedure.[6] It is well known that doping Mn^{2+} ions into the ZnS lattice can give rise to the strong yellow-orange light emission located at about 583 nm (through the $^4T_1$ to $^6A_1$ internal transition) with a high quantum yield, the luminescence lifetime of which is about 1 ms.[7] Such a strong luminescence and long lifetime allows the light penetrate into and out of the tissues and distinguish the luminescence from the background autofluorescence. These excellent optical properties make ZnS:Mn^{2+} nanocrystals potential candidates for fluorescent labeling agents. Magnetic Fe_3O_4 nanoparticles are the most prominent class of magnetic nanoparticles (MNPs) for their biocompatibility and stability.[8–10] At diameters less than 10 nm, Fe_3O_4 MNPs have unique properties such as high surface area, superparamagnetism and low Curie temperature *etc.*, and smaller particles may undergo rapid biodegradation when they are directly exposed to biological environments.[11,12] Therefore, bifunctional optical-magnetic ZnS:Mn^{2+}/Fe_3O_4 nanocomposites are highly desired in the biological field due to their appealing applications. However, fluorescence quenching always occurs due to the energy-transfer process between the ZnS:Mn^{2+} and Fe_3O_4.[13] To solve the problem, some transition layers, *e.g.* silica, polymer *etc.* have been used in the synthesis of the core–shell nanomaterials.[14–16] However, so far, the resultant nanocomposites are usually larger, and the synthetic procedure is rather complex and time-consuming. So, covalent linking between the ZnS:Mn^{2+} and Fe_3O_4 is highly desired to attenuate the energy-transfer process and increase the stability of the nanocomposites.[17] For further bioimaging applications, it is required to transfer the hydrophobic nanocomposites to water by surface modification, such as polymer, silica, or carbon coating techniques.[18–20] Among them, silica coating has attracted a great deal of attention because of its excellent chemical stability, biocompatibility and facile further conjugation with various functional groups.[21] To date, only a few

[a]*Institute of Condensed State Physics, Jilin Normal University, Siping 136000, P. R. China. E-mail: caojian_928@163.com; jhyang1@jlnu.edu.cn; Fax: +86 434 3294566; Tel: +86 434 3290009*
[b]*Key Laboratory of Functional Materials Physics and Chemistry of the Ministry of Education, Jilin Normal University, Siping 136000, P. R. China*
[c]*Changchun Institute of Optics, Fine Mechanics and Physics, Chinese Academy of Sciences, Changchun 130033, P. R. China*
[d]*University of Chinese Academy of Sciences, Beijing 100049, P. R. China*

methods have been reported for the preparation of water-soluble silica-coated nanocomposites with a size below 20 nm.

In this paper, we firstly designed a facile approach for fabricating bi-functional optical-magnetic ZnS:Mn^{2+} nanowires (NWs) decorated by Fe_3O_4 quantum dots (QDs) with different thickness of SiO_2 without using other components as the transition layer. The thioglycolic acid modified ZnS:Mn^{2+} NWs were conjugated with the citric acid modified Fe_3O_4 QDs to form stable nanocomposites through the reaction between the hydroxyl groups on the surface of the QDs and the carboxyl groups modified on the surface of the NWs. The effects of the surface modification and SiO_2 thickness on the optical and superparamagnetic properties of the nanocomposites were investigated.

Experimental section

Materials

Zinc nitrate, manganese nitrate, thiourea, ethylenediamine (EN), thioglycolic acid (MPA), ferric chloride ($FeCl_3 \cdot 6H_2O$), ferrous chloride ($FeCl_2 \cdot 4H_2O$), PEG-4000, ethylene glycol, concentrated ammonia aqueous solution (25%), citric acid, tetraethyl orthosilicate (TEOS) and ethanol were all analytical grade (Shanghai Chemical Reagents Co.), and used without further purification.

Preparation and chemical modification of ZnS:Mn^{2+} (1%) NWs

In a typical process, 0.99 mmol of zinc nitrate and 0.01 mmol of manganese nitrate were dissolved in 16 ml EN and water (1 : 1 in volume ratio). After stirring for 1 hour, 3 mmol of thiourea was added to the resulting complex. After stirring for 2 hours, the colloid solution was transferred into a 20 ml Teflon-lined autoclave and kept at 180 °C for 12 hours. After the reaction, the autoclave was taken out and cooled down to room temperature. The product was washed with ethanol and deionized water for several times and separated by centrifugation, and then dried at 80 °C for 1 hour to yield a white powder.

ZnS:Mn^{2+} (1%) NWs was modified with MPA as follows: 9.7 mg of ZnS:Mn^{2+} NWs were dispersed ultrasonically in deionized water (100 ml), and then 75 μl of MPA was added to the above solution under magnetic stirring for 1 hour to form the ZnS:Mn^{2+}(–SH) water solution.

Preparation and chemical modification of Fe_3O_4 QDs

Fe_3O_4 QDs were prepared through an improved chemical coprecipitation method. $FeCl_3 \cdot 6H_2O$ (6 mmol), $FeCl_2 \cdot 4H_2O$ (10 mmol) and PEG-4000 (10 g) were dissolved in absolute ethylene glycol (250 ml). After stirring for 30 min at room temperature, 100 ml of concentrated ammonia aqueous solution (25%) was added rapidly to the resulting complex. Then the reaction mixture was heated at 110 °C for 2 hours under mechanical stirring, producing a black and homogeneous suspension. After cooling to room temperature, the precipitate was separated with a permanent magnet and washed with deionized water and ethanol for several times until the pH decreased to 7.0, followed by drying in a vacuum oven at 40 °C for 48 hours.

Fe_3O_4 QDs was modified with citric acid as follows: 0.023 g of Fe_3O_4 QDs and 0.023 g of citric acid were dispersed in 250 ml of deionized water under mechanical stirring for 1 hour to form the Fe_3O_4(–COOH) water solution.

Preparation of ZnS:Mn^{2+}(–SH) NWs/Fe_3O_4(–COOH) QDs/SiO_2 core–shell nanostructures

100 ml of ZnS:Mn^{2+}(–SH) water solution and 250 ml of Fe_3O_4 (–COOH) water solution were mixed in a three-necked flask under mechanical stirring for 1 hour. A mixed solution including 50 ml of absolute alcohol, 1 ml of distilled water, 1.7 ml of aqueous ammonia, and 200 μl of TEOS was injected into the above solution. The mixture was continuously stirred for 5 hours at room temperature. The product was washed with ethanol several times and separated by centrifugation, and then dried at 60 °C for 3 hours to obtain a powder. To investigate the effects of the SiO_2 thickness on the optical and magnetic properties of the samples, a set of samples were synthesized at different time periods (t = 1, 3, 7 hours). The same process was carried out except for using the ZnS:Mn^{2+} and Fe_3O_4 to displace the ZnS:Mn^{2+}(–SH) and Fe_3O_4(–COOH) for comparison.

Characterization of products

X-ray diffraction (XRD) patterns were collected on a MAC Science MXP-18 X-ray diffractometer using a Cu target radiation source. Transmission electron micrographs (TEM) and high-resolution transmission electron microscopy (HRTEM) images were taken on a JEM-2100 electron microscope. The specimen was prepared by depositing a drop of the dilute solution of the sample in ethanol on a carbon-coated copper grid and drying at room temperature. EDAX microanalysis was performed at the SEM magnification. Fourier transform infrared (FT-IR) spectra were recorded on a Bruker Vertex 70 spectrophotometer in KBr pellets. Photoluminescence (PL) measurements were carried out at room temperature, using 325 nm as the excitation wavelength and a He–Cd laser as the source of excitation. Magnetic hysteresis loop was measured by a Lake Shore 7407 vibrating sample magnetometer (VSM) with the maximum field of 6 kOe. The samples used for the XRD, EDAX, FT-IR, PL and VSM measurements were solid powders.

The quantum yield (QY) of the sample was measured relative to the organic dye Rhodamine B (5.0 μg mL^{-1}) in ethanol solution (QY = 95%), which can be determined from the following equation:

$$QY_x = QY_s \left[\frac{E_x}{E_s}\right] \left[\frac{A_s}{A_x}\right] \left[\frac{n_x}{n_s}\right]^2$$

In the equation, E_x (sample) and E_s (standard) are the integrated emission peak areas, A_x (sample) and A_s (standard) are the absorbance at the excitation wavelength, and n_x (sample) and n_s (standard) are the refractive indices of the solvents: $n_{ethanol}$ is 1.359 and n_{water} is 1.333 at room temperature. UV-Vis absorption spectrum was measured on a UV-3101PC UV spectrometer. PL spectrum was taken using a fluorescence spectrophotometer (Perkin-Elmer, LS55) at room temperature. The specimen for the

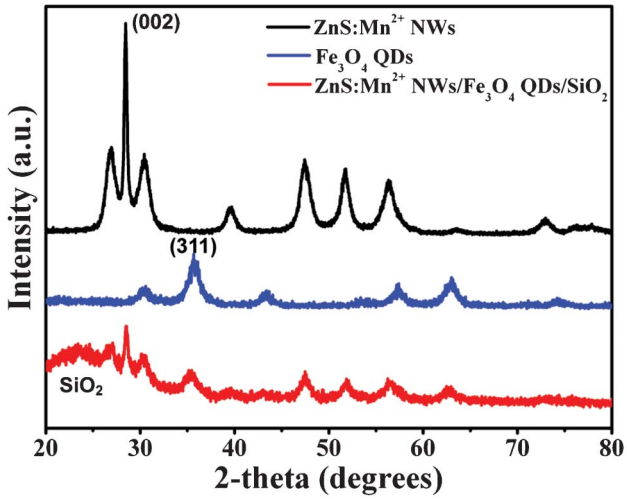

Fig. 1 XRD patterns of ZnS:Mn^{2+} NWs (black line); Fe_3O_4 QDs (blue line); ZnS:Mn^{2+}(SH)/Fe_3O_4(COOH)/SiO_2 nanocomposites (red line).

measurement was dispersed in water and placed in a 1 cm quartz cell, and water served as the reference. In order to reduce the measurement error, multiple concentrations were examined for the sample, and the optical densities at the excitation wavelengths of both Rhodamine B and the sample solution were set to be always below 0.08 to minimize the reabsorption effect.

Results and discussion

Fig. 1 shows the XRD patterns of the ZnS:Mn^{2+} NWs, Fe_3O_4 QDs and ZnS:Mn^{2+}(SH)/Fe_3O_4(COOH)/SiO_2 nanocomposites. As seen from Fig. 1 black line, all the diffraction peaks for the ZnS:Mn^{2+} NWs can be well indexed as the hexagonal wurtzite phase structure, which are consistent with the standard card (JCPDS No. 36-1450). No impurity phase can be found in the spectrum, indicating that the Mn^{2+} ions have been incorporated into the ZnS lattice. It is possible to predict the growth direction by comparing the full width at half maximum (FWHM) for different XRD peaks. It is noticeable that the (002) diffraction peak is stronger and narrower than the other peaks, suggesting a preferential growth direction along the *c*-axis.[22] In the case of the Fe_3O_4 QDs (Fig. 1 blue line), all the diffraction peaks can be indexed as the face-centered cubic structure, which are consistent with the standard card (JCPDS No. 19-0629). The average size estimated from the FWHM using the Debye–Scherrer formula[23] is about 5 nm. The XRD pattern of the ZnS:Mn^{2+}(SH)/Fe_3O_4(COOH)/SiO_2 nanocomposites (Fig. 1 red line) shows the characteristic peak of the amorphous SiO_2 in addition to that of the ZnS:Mn^{2+} and Fe_3O_4, indicating that the sample is a composite material including the ZnS:Mn^{2+} NWs, Fe_3O_4 QDs and SiO_2. Additionally, all the diffraction peaks for the ZnS:Mn^{2+}(SH)/Fe_3O_4(COOH)/SiO_2 nanocomposites (red line) are much weaker than those of the ZnS:Mn^{2+} NWs (black line), which may be due to the formation of the core–shell structure.

The detailed microstructures of the prepared samples are characterized using transmission electron microscopy. Fig. 2a and b display the TEM, EDAX and HRTEM images of the ZnS:Mn^{2+} NWs. The HRTEM image (Fig. 2b) was taken from the area marked by the red rectangle in Fig. 2a. It can be seen that the ZnS:Mn^{2+} NWs are smooth and the diameter is about 6–8 nm. The growth direction of the ZnS:Mn^{2+} NWs is perpendicular to the lattice fringes, and the *d* spacing of the (002) plane is about 0.31 nm.[24] The EDAX image of the ZnS:Mn^{2+} NWs (the inset figure in Fig. 2a) shows that the sample contains Zn, S and Mn elements, 0.56 at% Mn can be detected for the ZnS:Mn^{2+} (1%) NWs. Fig. 2c and d show the TEM, size distribution histogram and HRTEM images of the Fe_3O_4 QDs. It can be seen that these QDs are well crystallized and the average diameter of the QDs is about 4–5 nm. The lattice fringes with the *d* spacing of 0.25 nm can be assigned to the (311) plane of the cubic Fe_3O_4 QDs,[6,25] which is consistent with the XRD results.

Fig. 3 displays the TEM and HRTEM images of the ZnS:Mn^{2+}(SH)/Fe_3O_4(COOH)/SiO_2 nanocomposites. The TEM image (Fig. 3a) shows an apparent contrast between the inner core and the outer shell, the QDs assemble uniformly around the surface of the NWs, which suggests the existence of the core–shell structure. The average diameter of the ZnS:Mn^{2+}(SH)/Fe_3O_4(COOH)/SiO_2 nanocomposites is about 18 nm, which is not obviously enlarged, revealing that the SiO_2 layer is thin. The different lattice fringes between the Fe_3O_4 QDs and ZnS:Mn^{2+} NWs can be clearly identified in the HRTEM image (Fig. 3b) taken from the area marked by the red rectangle in Fig. 3a, which provides strong evidence for the composite nature of the sample.

Fig. 4 shows the proposed formation mechanism of the ZnS:Mn^{2+}(SH)/Fe_3O_4(COOH)/SiO_2 nanocomposites. For the ZnS:Mn^{2+} NWs modified by MPA, thiol groups (–SH) can form stable bonds with the metals (Zn^{2+}) with the carboxyl groups (–COOH) protruding outwards from the surface of the NWs.[26,27] Fe_3O_4 QDs are functionalized with citric acid, the surface of which are modified by carboxyl groups (–COOH) and hydroxyl groups (–OH). After mixing the ZnS:Mn^{2+} NWs and Fe_3O_4 QDs together, the QDs can be covalently bonded to the NWs by the –COO groups in order to avoid the charge transfer from the ZnS:Mn^{2+} NWs to the Fe_3O_4 QDs, thereby retaining both the fluorescence and magnetic properties. Subsequently, silica is coated on the surface of Fe_3O_4 QDs to form the ZnS:Mn^{2+}(SH)/Fe_3O_4(COOH)/SiO_2 nanocomposites through the hydrolysis of TEOS according to the Stöber method.[28] The SiO_2 shell can effectively prevent the aggregation and chemical degradation of the ZnS:Mn^{2+}/Fe_3O_4 nanocomposites in a harsh liquid environment.

FT-IR spectra were recorded and used to identify the changes of the functional groups on the surface of the nanocomposites. For the Fe_3O_4 QDs (red line in Fig. 5), the vibration of the Fe–O bonds centered at 585.9 cm^{-1} is the characteristic absorption of the Fe_3O_4.[6,29] For the ZnS:Mn^{2+}/Fe_3O_4/SiO_2 nanocomposites (green line in Fig. 5), the strong peak at 1095.7 cm^{-1} can be assigned to the vibration of the Si–

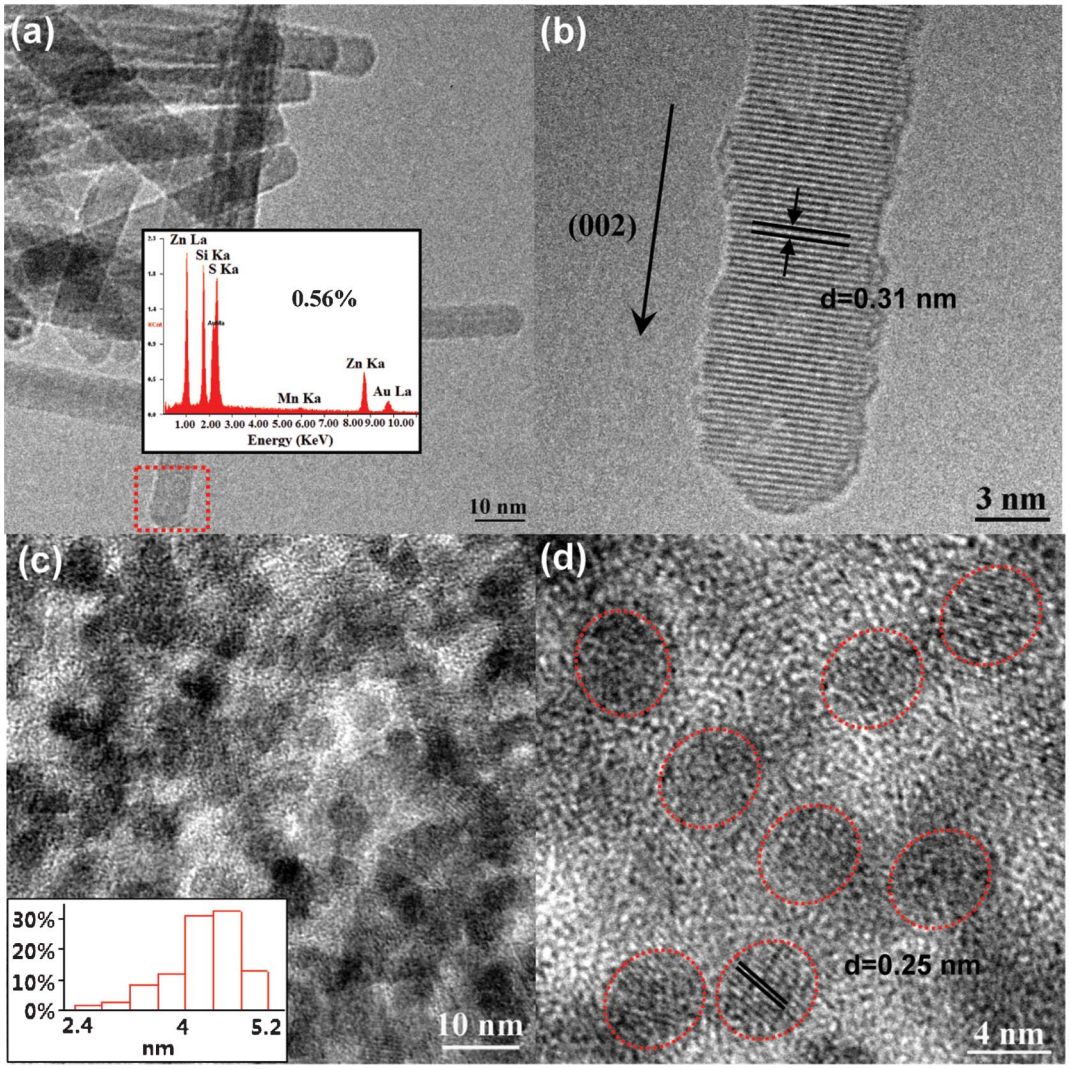

Fig. 2 (a, b) TEM and HRTEM images of the ZnS:Mn^{2+} (1%) NWs, the inset figure of (a) is the EDAX image of the ZnS:Mn^{2+} (1%) NWs; (c, d) TEM and HRTEM images of the Fe_3O_4 QDs, the inset figure of (c) is the size distribution histogram of the Fe_3O_4 QDs obtained from counting 100 QDs.

O bonds, demonstrating the existence of the SiO_2 components.[30] For the ZnS:Mn^{2+}(SH)/Fe_3O_4(COOH)/SiO_2 nanocomposites (blue line in Fig. 5), the two peaks at 1406 and 1576 cm^{-1} correspond to the stretching vibration of the carboxyl, which indicates that the citric acid have been successfully modified on the surface of the Fe_3O_4 QDs.[15] For three samples, a strong peak at 3411 cm^{-1} can be observed, which is ascribed to the stretching vibration of the O–H bonds in water.[17,31] Moreover, the intensity of the Fe–O bonds for the ZnS:Mn^{2+}/Fe_3O_4/SiO_2 and ZnS:Mn^{2+}(SH)/Fe_3O_4(COOH)/SiO_2 nanocomposites is much lower than that for the Fe_3O_4 QDs, which further proves that the Fe_3O_4 QDs have been coated by citric acid and SiO_2.

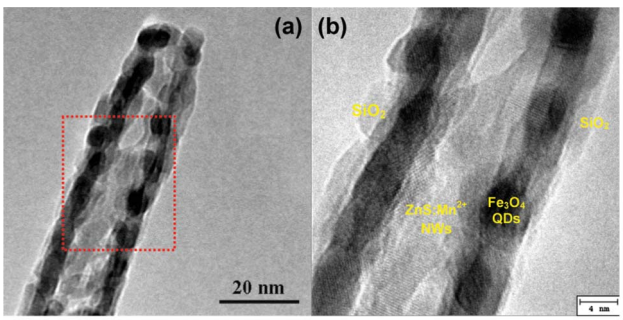

Fig. 3 (a, b) TEM and HRTEM images of the ZnS:Mn^{2+}(SH)/Fe_3O_4(COOH)/SiO_2 nanocomposites.

Surface modification always plays a critical role in determining the optical properties of the nanocrystals. Fig. 6a shows the room temperature PL spectra of the ZnS:Mn^{2+} NWs, ZnS:Mn^{2+}/Fe_3O_4/SiO_2, ZnS:Mn^{2+}(SH)/Fe_3O_4/SiO_2, and ZnS:Mn^{2+}(SH)/Fe_3O_4(COOH)/SiO_2 nanocomposites. The PL spectrum of the ZnS:Mn^{2+} NWs (black line in Fig. 6a) shows a strong yellow-orange emission peak at 585 nm (corresponding to the Mn^{2+} $^4T_1$–$^6A_1$ transition), indicating

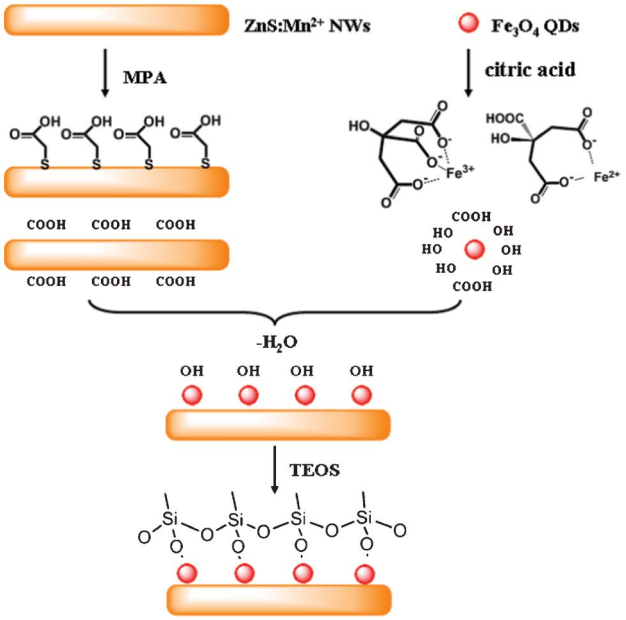

Fig. 4 Schematic illustration of the formation mechanism of the water-soluble ZnS:Mn^{2+}(SH)/Fe_3O_4(COOH)/SiO_2 nanocomposites.

that the Mn^{2+} ions have been successfully incorporated into the ZnS lattice.[32] After embedding the ZnS:Mn^{2+} NWs and Fe_3O_4 QDs together within the SiO_2 matrix, the intensity of the yellow-orange emission (red line in Fig. 6a) is approximately three times lower than that of the unpassivated counterpart

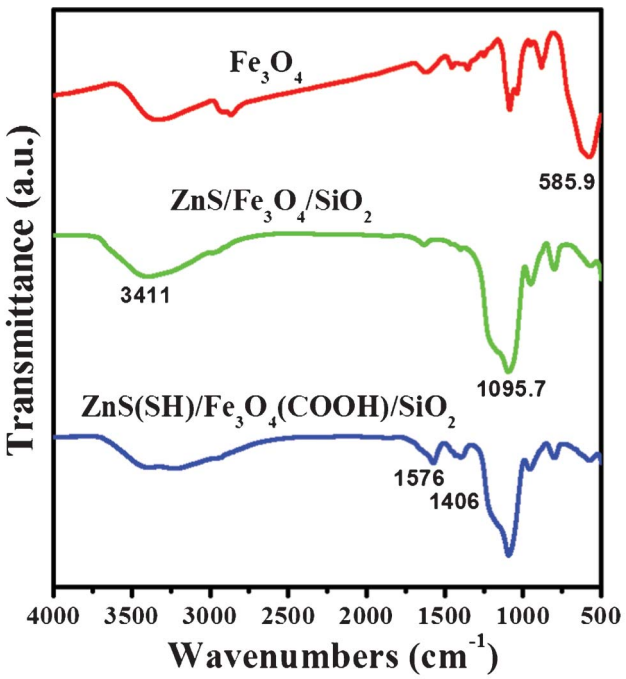

Fig. 5 FT-IR spectra of the Fe_3O_4 QDs (red line); ZnS:Mn^{2+}/Fe_3O_4/SiO_2 nanocomposites (green line); ZnS:Mn^{2+}(SH)/Fe_3O_4(COOH)/SiO_2 (blue line) nanocomposites.

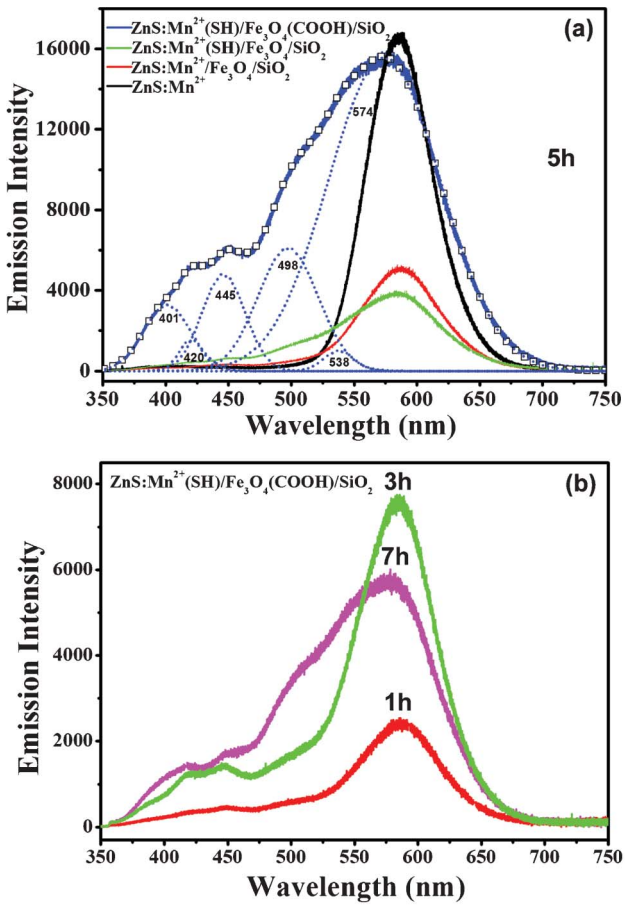

Fig. 6 Room temperature PL spectra of (a) ZnS:Mn^{2+} NWs (black line), ZnS:Mn^{2+}/Fe_3O_4/SiO_2 (red line), ZnS:Mn^{2+}(SH)/Fe_3O_4/SiO_2 (green line), and ZnS:Mn^{2+}(SH)/Fe_3O_4(COOH)/SiO_2 (blue line) nanocomposites with the SiO_2 growth time of 5 h; (b) ZnS:Mn^{2+}(SH)/Fe_3O_4(COOH)/SiO_2 nanocomposites with the SiO_2 growth time of 1, 3 and 7 h.

(black line in Fig. 6a). Since that the interaction between the ZnS:Mn^{2+} NWs and Fe_3O_4 QDs would lead to the energy transfer from the NWs to the QDs, hence reduce the PL intensity. After coating –SH groups on the surface of the NWs, the intensity of the ZnS:Mn^{2+}(SH)/Fe_3O_4/SiO_2 nanocomposites is further decreased (green line in Fig. 6a). Zheng *et al.* have pointed out that the thiol ligands acted as the PL quencher for the ZnS:Mn^{2+} QDs due to the lower energy levels of the valence band (−1.78 eV) compared to the highest occupied molecular orbital levels of the thiol ligands (−1.0 eV).[33–35] It is worth noting that the PL intensity of the as-synthesized ZnS:Mn^{2+}(SH)/Fe_3O_4(COOH)/SiO_2 nanocomposites (blue line in Fig. 6a) is comparable to that of the ZnS:Mn^{2+} NWs (black line in Fig. 6a) after modifying the Fe_3O_4 QDs with citric acid. The PL enhancement can be attributed to the following factors: firstly, the dominant mechanism could be the changed surface structure and the effective surface passivation induced by the ligand exchange.[33] So there would be more energy transfer from the hosts to the d-orbital of the Mn^{2+} ions than that to the nonradiative recombination centers on the surface

of the ZnS:Mn^{2+} NWs; secondly, the ligands (–OH, –COOH, –COO) between the NWs and QDs can serve as an extra barrier for confining the electrons to the interior of the NWs, which could increase the possibility of the electrons to fall into the d-orbital, and subsequently enhance the dopant emission.[36] Moreover, the QY of the ZnS:Mn^{2+}(SH)/Fe_3O_4(COOH)/SiO_2 nanocomposites is calculated to be 20 $\pm$ 1%, indicating that the nanocomposites possess high quality luminescent properties. In addition, the PL spectrum of the ZnS:Mn^{2+}(SH)/Fe_3O_4(COOH)/SiO_2 nanocomposites becomes asymmetric due to the joints between the NWs and QDs, which is consistent with the results of CdS/Fe_3O_4 heterostructures.[37] It can be deconvoluted into six Gaussian peaks centered at 401, 420, 445, 498, 538, 574 nm, respectively. According to the energy diagram of the defects distributed in the ZnS, the emission peaks can be attributed to the following origins: 401 nm to the sulfur vacancy and interstitial sulfur lattice defects,[38] 420 and 445 nm to the sulfur vacancy and surface states,[39,40] 498 nm to the self-activated defect centers formed by the zinc vacancy inside the lattice,[24] 538 nm to the sulfur species on the surface of the ZnS NWs,[41] and 574 nm to the Mn^{2+} $^4T_1$–$^6A_1$ transition.[42] It is noticeable that the yellow-orange emission shifts from 585 nm to 574 nm after modifying the Fe_3O_4 QDs with citric acid, *i.e.* blue shift occurs. The interactive straining caused by the large variation in lattice parameters between the core and shell may lead to the blue shift of the yellow-orange emission.

To investigate the effect of the SiO_2 shell thickness on the optical properties of the ZnS:Mn^{2+}(SH)/Fe_3O_4(COOH)/SiO_2 nanocomposites, the PL spectra of the samples grown at different times are shown in Fig. 6b. For the yellow-orange emission, the PL intensity keeps increasing until t = 5 h and then decreases rapidly when the time continually increases to 7 h. The PL intensity of the emission is mainly determined by the degree of surface passivation. At the early stage of the hydrolysis of TEOS, only parts of ZnS:Mn^{2+} NWs and Fe_3O_4 QDs were encapsulated by the silica shell, while the rest of the ZnS:Mn^{2+} NWs and Fe_3O_4 QDs still remained in the solution, which can be removed in the experiment. So, the surface of the ZnS:Mn^{2+} NWs and Fe_3O_4 QDs can be passivated fully by the Fe_3O_4 QDs and SiO_2, respectively. With the increase in the hydrolysis time of TEOS, the silica shell became thick and more ZnS:Mn^{2+} NWs and Fe_3O_4 QDs would be encapsulated. But the thick Fe_3O_4 and SiO_2 coating would induce strain at the interface caused by the lattice mismatch between one another. It would result in new traps for carriers, which are thought to be the main reason for the decrease of the yellow-orange emission after t = 5 h.

The magnetic properties of the Fe_3O_4 QDs, the ZnS:Mn^{2+}(SH)/Fe_3O_4(COOH)/SiO_2 nanocomposites with different SiO_2 thickness, ZnS:Mn^{2+}(SH)/Fe_3O_4/SiO_2 and ZnS:Mn^{2+}/Fe_3O_4/SiO_2 nanocomposites measured at room temperature are shown in Fig. 7. All of the samples exhibit superparamagnetic properties, where negligible coercivity and remanence in the magnetization curves are observed and the magnetic moments are only induced in the presence of a magnetic field. The magnetic saturation (M_s) value of the Fe_3O_4 QDs is 20 emu g^{-1} (Fig. 7a), which is lower than that of the bulk Fe_3O_4 (92 emu g^{-1}).[43] Since the saturation magnetization as well as the magnetic moment of the particle is proportional to its size,[44] hence the as-synthesized Fe_3O_4 QDs exhibit the smaller M_s. However, the M_s value is reduced largely in the presence of ZnS:Mn^{2+} NWs and amorphous SiO_2 compared with the Fe_3O_4 QDs (Fig. 7b and c), which is

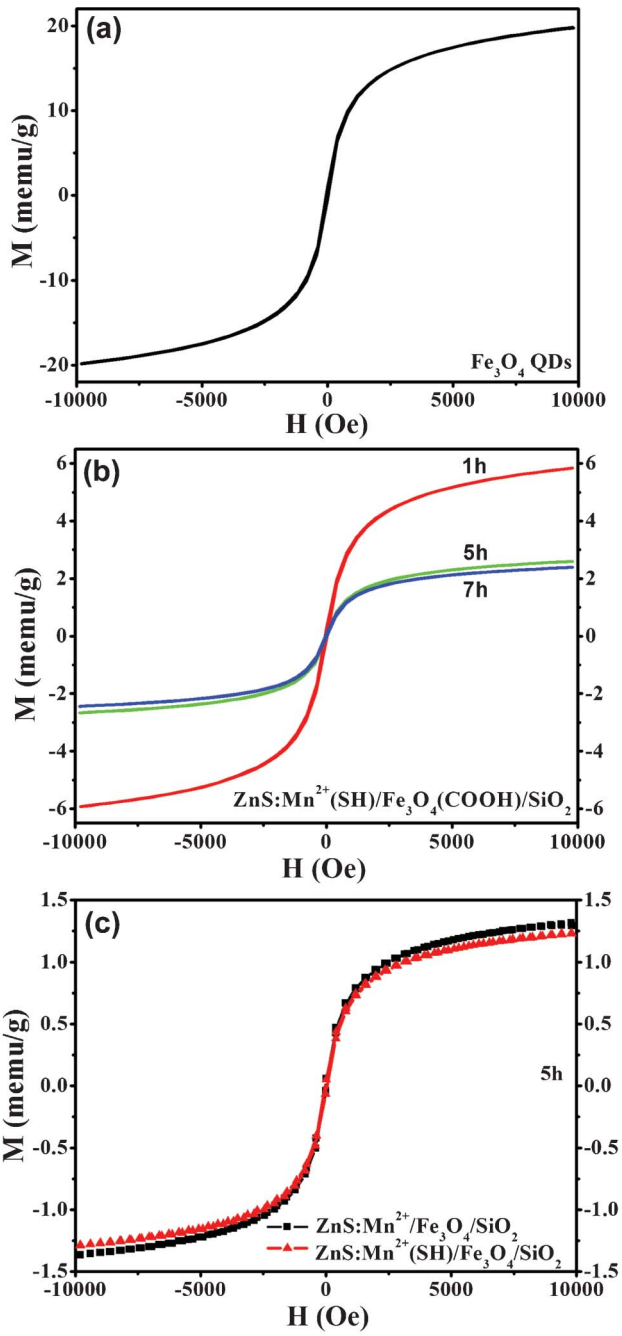

Fig. 7 Magnetic hysteresis loops of (a) Fe_3O_4 QDs; (b) ZnS:Mn^{2+}(SH)/Fe_3O_4(COOH)/SiO_2 nanocomposites with the SiO_2 growth time of 1, 5 and 7 h; (c) ZnS:Mn^{2+}/Fe_3O_4/SiO_2 and ZnS:Mn^{2+}(SH)/Fe_3O_4/SiO_2 nanocomposites with the growth time of 5 h.

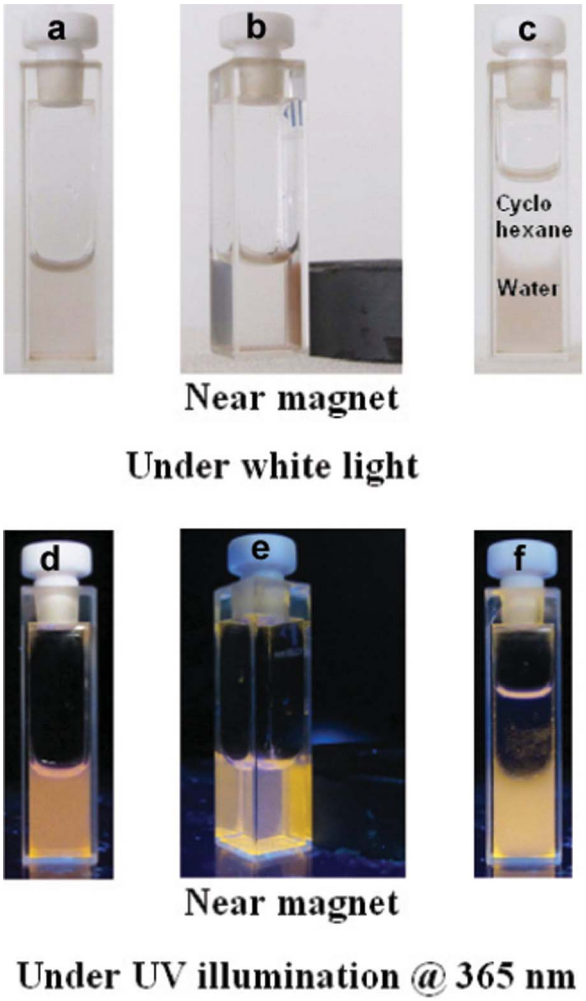

Fig. 8 Photographic images of a water solution of the ZnS:Mn^{2+}(SH)/Fe_3O_4(COOH)/SiO_2 nanocomposites under white light (a) without and (b) with a magnetic field) and UV illumination (λ = 365 nm) ((d) without and (e) with a magnetic field); (c, f) photographic images of the water and cyclohexane solution of the ZnS:Mn^{2+}(SH)/Fe_3O_4(COOH)/SiO_2 nanocomposites under white light and UV illumination (λ = 365 nm).

consistent with the literature.[45] For the ZnS:Mn^{2+}(SH)/Fe_3O_4(COOH)/SiO_2 nanocomposites (Fig. 7b), the M_s is decreased as the thickness of the SiO_2 increased, which is mainly due to the lower mass content of Fe_3O_4 in the nanocomposites as the mass of the SiO_2 increased.[45] It is noted that the surface modification also play an important role in affecting the magnetic properties, which can be seen in Fig. 7c. The decreased M_s value for the ZnS:Mn^{2+}(SH)/Fe_3O_4/SiO_2 and ZnS:Mn^{2+}/Fe_3O_4/SiO_2 nanocomposites compared with the ZnS:Mn^{2+}(SH)/Fe_3O_4(COOH)/SiO_2 nanocomposites can be attributed to the surface spin disorder due to capping.[13] In addition, surface modification can also make the NWs load more QDs on its surface by the stable covalent bonds.

Fig. 8 shows the photographic images of the ZnS:Mn^{2+}(SH)/Fe_3O_4(COOH)/SiO_2 nanocomposites under white light and UV illumination (λ = 365 nm) with and without an external magnetic field. It can be seen that the solution of the as-synthesized nanocomposites is orange and the nanocomposites are well dispersed in the aqueous solution under white light (Fig. 8a and c) and UV irradiation (Fig. 8d and f). When a permanent magnet is placed near the solution (Fig. 8b and e), the nanocomposites are attracted and accumulated toward the magnet, eventually leaving a clear solution behind, indicating that the magnetic separation occurs. From the optical and magnetic properties of the nanocomposites, it can be concluded that the ZnS:Mn^{2+}(SH)/Fe_3O_4(COOH)/SiO_2 nanocomposites show the strong fluorescent emission and desired superparamagnetic properties, which enable them to serve as multifunctional nanocomposites with promising applications in biological imaging, magnetic guiding and separation.

Conclusions

In this paper, the water-soluble ZnS:Mn^{2+}(SH)/Fe_3O_4(COOH)/SiO_2 nanocomposites were fabricated successfully by assembling the citric acid capped Fe_3O_4 QDs on MPA-coated ZnS:Mn^{2+} NWs by the Stöber method. The effects of the surface modification and SiO_2 thickness on its optical and magnetic properties were studied. It was found that the citric acid coating on the surface of the Fe_3O_4 QDs could effectively suppress the interaction between the ZnS:Mn^{2+} NWs and Fe_3O_4 QDs. The presented water-soluble core–shell nanocomposites offer the excellent yellow-orange emission of the ZnS:Mn^{2+} NWs and retain the superparamagnetic properties of the Fe_3O_4 QDs. Therefore, the fluorescent, superparamagnetic and water-soluble properties of the ZnS:Mn^{2+}(SH)/Fe_3O_4(COOH)/SiO_2 nanocomposites would allow them to find applications in biolabeling, bioseparation and diagnostic analysis.

Acknowledgements

This work was financially supported by the National Natural Science Foundation of China (Grant No. 61008051, 61178074, 11204104, 11254001).

References

1 N. Cho, T. Cheong, J. H. Min, J. Wu, S. J. Lee, D. Kim, J. Yang, S. Kim, Y. K. Kim and S. Seong, *Nat. Nanotechnol.*, 2011, **675**, 6.
2 M. Yang, K. Cheng, S. Qi, H. Liu, Y. Jiang, H. Jiang, J. Li, K. Chen, H. Zhang and Z. Cheng, *Biomaterials*, 2013, **34**, 2796.
3 S. Jiang, A. A. Eltoukhy, K. T. Love, R. Langer and D. G. Anderson, *Nano Lett.*, 2013, **13**, 1059.
4 C. Lee, H. H. Chang, P. Bae, J. Jung and B. H. Chung, *Macromol. Biosci.*, 2013, **13**, 321.
5 Z. Wang, G. Cheng, Y. Liu, J. Zhang, D. Sun and J. Ni, *J. Mater. Chem. B*, 2013, **1**, 1491.

6 X. Yu, J. Wan, Y. Shan, K. Chen and X. Han, *Chem. Mater.*, 2009, **21**, 4892.
7 L. Liu, L. Xiao and H. Zhu, *Chem. Phys. Lett.*, 2012, **539–540**, 112.
8 S. L. C. Pinho, G. A. Pereira, P. Voisin, J. Kassem, L. Etienne, J. A. Peters, L. Carlos and C. F. G. C. Geraldes, *ACS Nano*, 2010, **4**, 5339.
9 R. Hao, R. Xing, Z. Xu, Y. Hou, S. Gao and S. Sun, *Adv. Mater.*, 2010, **22**, 2729.
10 P. Yi, G. Chen, H. Zhang, F. Tian, B. Tan, J. Dai, Q. Wang and Z. Deng, *Biomaterials*, 2013, **34**, 3010.
11 P. Jiang, X. Yang, Y. Xin, Y. Qi, X. Ma, Q. Li and Z. Zhang, *J. Mater. Sci.*, 2012, **48**, 2365.
12 Y. Xu, A. Karmakar, D. Wang, M. W. Mahmood, F. Watanabe, Y. Zhang, A. Fejleh, P. Fejleh, Z. Li, G. Kannarpady, S. Ali, A. R. Biris and A. S. Biris, *J. Phys. Chem. C*, 2010, **114**, 5020.
13 A. Kale, S. Kale, P. Yadav, H. Gholap, R. Pasricha, J. P. Jog, B. Lefez, P. Shastry and S. Ogale, *Nanotechnology*, 2011, **22**, 225101.
14 Z. Wang, S. Zhu, S. Zhao and H. Hu, *J. Alloys Compd.*, 2011, **509**, 6893.
15 C. Tu, Y. Yang and M. Gao, *Nanotechnology*, 2008, **19**, 105601.
16 Y. Lu, Y. Yin, B. T. Mayers and Y. Xia, *Nano Lett.*, 2002, **2**, 183.
17 P. Sun, H. Zhang, C. Liu, J. Fang, M. Wang, J. Chen, J. Zhang, C. Mao and S. Xu, *Langmuir*, 2010, **26**, 1278.
18 S. Biswajit, V. Vinithra, A. M. Bodratti, T. Marina and A. Paschalis, *J. Colloid Interface Sci.*, 2013, **397**, 1.
19 M. Gema, P. Ernesto, C. Teresa and P. Carmen, *J. Phys. Chem. C*, 2011, **115**, 25247.
20 J. Wang, Y. Zhao, F. Ma, K. Wang, F. Wang and X. Xia, *J. Mater. Chem. B*, 2013, **1**, 1406.
21 H. L. Ding, Y. X. Zhang, S. Wang, J. M. Xu, S. C. Xu and G. H. Li, *Chem. Mater.*, 2012, **24**, 4572.
22 S. Kar, S. Santra and H. Heinrich, *J. Phys. Chem. C*, 2008, **112**, 4036.
23 P. V. B. Lakshmi, K. S. Raj and K. Ramachandran, *Cryst. Res. Technol.*, 2009, **44**, 153.
24 S. Biswas, S. Kar and S. Chaudhuri, *J. Phys. Chem. B*, 2005, **109**, 17526.
25 J. Su, M. Cao, L. Ren and C. Hu, *J. Phys. Chem. C*, 2011, **115**, 14469.
26 B. A. Harruff and C. E. Bunker, *Langmuir*, 2003, **19**, 893.
27 W. Guo, J. J. Li, Y. A. Wang and X. Peng, *J. Am. Chem. Soc.*, 2003, **125**, 3901.
28 W. Stöber, A. Fink and E. Bohn, *J. Colloid Interface Sci.*, 1968, **26**, 62.
29 M. Zhu and G. Diao, *J. Phys. Chem. C*, 2011, **115**, 18923.
30 L. Zhou, C. Gao and W. Xu, *Langmuir*, 2010, **26**, 11217.
31 J. Dai, S. Wu, W. Jiang, P. Li, X. Chen, L. Liu, J. Liu, D. Sun, W. Chen, B. Chen and F. Li, *J. Magn. Magn. Mater.*, 2013, **331**, 62.
32 J. Cao, J. Yang, L. Yang, M. Wei, B. Feng, D. Han, L. Fan, B. Wang and H. Fu, *J. Appl. Phys.*, 2012, **112**, 014316.
33 J. Zheng, F. Gao, G. Wei and W. Yang, *Chem. Phys. Lett.*, 2012, **519–520**, 73.
34 P. Shao, Q. Zhang, Y. Li and H. Wang, *J. Mater. Chem.*, 2011, **21**, 151.
35 J. V. Lker, X. Zhou, X. Ma, S. Flessau, H. Lin, M. Schmittel and A. Mews, *Angew. Chem., Int. Ed.*, 2010, **49**, 6865.
36 L. E. Brus, *J. Chem. Phys.*, 1983, **79**, 5566.
37 L. Wang, H. Wei, Y. Fan, X. Gu and J. Zhan, *J. Phys. Chem. C*, 2009, **113**, 14119.
38 P. Hu, Y. Liu, L. Fu, L. Cao and D. Zhu, *J. Phys. Chem. B*, 2004, **108**, 936.
39 Y. Li, X. Li, C. Yang and Y. Li, *J. Phys. Chem. B*, 2004, **108**, 16002.
40 S. Kar, S. Biswas and S. Chaudhuri, *Nanotechnology*, 2005, **16**, 3074.
41 Z. Li, B. Liu, X. Li, S. Yu, L. Wang, Y. Hou, Y. Zou, M. Yao, Q. Li, B. Zou, T. Cui, G. Zou, G. Wang and Y. Liu, *Nanotechnology*, 2007, **18**, 255602.
42 J. Ge, J. Wang, H. Zhang, X. Wang, Q. Peng and Y. Li, *Adv. Funct. Mater.*, 2005, **15**, 303.
43 C. J. Jia, L. D. Sun, F. Luo, X. D. Han, L. J. Heyderman, Z. G. Yan, C. H. Yan, K. Zheng, Z. Zhang, M. Takano, N. Hayashi, M. Eltschka, M. Klaui, U. Rudiger, T. Kasama, L. Cervera-Gontard, R. E. Dunin-Borkowski, G. Tzvetkov and J. Raabe, *J. Am. Chem. Soc.*, 2008, **130**, 16968.
44 O. Song and Z. J. Zhang, *J. Am. Chem. Soc.*, 2004, **126**, 6164.
45 H. Hu, Z. Wang, L. Pan, S. Zhao and S. Zhu, *J. Phys. Chem. C*, 2010, **114**, 7738.

